A Finite-Element Thermoelectric model for Phase-Change Memory devices

Aravinthan Athmanathan*†, Daniel Krebs*, Abu Sebastian*, Manuel Le Gallo*,
Haralampos Pozidis* and Evangelos Eleftheriou*
*IBM Research – Zurich, 8803 Rüschlikon, Switzerland. e-mail: aat@zurich.ibm.com
†Microelectronics System Laboratory (LSM), EPFL, 1005 Lausanne, Switzerland.

***Abstract*—In this article, we present a finite-element method (FEM)-based thermo-electric model to accurately capture the characteristics of phase-change memory devices. The individual thermoelectric heating components are separated to obtain a detailed understanding of thermal transport in the device. This work is different from other exciting modeling work on thermoelectrics in that, for the first time, it compares the modeling results with experimental measurements obtained over a range of ambient temperatures, thereby validating the accuracy of the proposed model.**

I. Introduction

Phase Change Memory (PCM) has emerged as a successful candidate for future non-volatile memory (NVM) because of its extended scalability, high reliability, high endurance, moderate data retention and multi-bit per cell (MLC) storage capability. The materials used in PCM (typically $Ge_2Sb_2Te_5$, GST) exhibit high resistivity contrast between their two stable states, namely, the crystalline (low-resistive) and the amorphous (high-resistive) state, which can be exploited to store information [1].

Modeling of PCM devices plays a critical role in understanding the phase-change switching process to improve the device performance. Most commonly, the power for switching is solely attributed to the resistive Joule-heating (I^2R) generated by the applied current. However, some of the recent works revealed that apart from Joule-heating, also thermoelectric phenomena contribute significantly to the operating dynamics of PCM devices [2]–[4]. Given the current aggressive scaling trends, the thermoelectric effect plays an increasingly important role in smaller dimensions owing to the enhanced thermal confinement. Therefore, from a modeling perspective, it is necessary to have a precise understanding of the thermoelectric effects and their impact on the device characteristics.

In this article, a thorough analysis of the PCM device operation of the traditional mushroom cell topology has been conducted using a finite-element model implemented in COMSOL Multiphysics. The Poisson equation and the heat diffusion equations are modified such that the additional thermoelectric heating components, arising from the Seebeck coefficients of the materials, are included. Field- and temperature-dependent material parameters were used for the crystalline and amorphous phase-change material. The proposed model is able to capture the device characteristics accurately as can be seen from the comparison of the simulation results with those of the experimental measurements. Our work differs from previous modeling attempts on thermoelectrics in that it provides a detailed quantitative match to temperature-dependent current vs. voltage ($I-V$) and resistance vs. programming power ($R-P$) experimental data. The model provides valuable insights into device operation and also into the influence of the various material properties on the $I-V$ and $R-P$ curves to improve the efficiency and performance of the device, which can be exploited.

II. Thermoelectric model of PCM

A. Theory

Besides phase-change kinetics, the coupled transport of heat and electrical current determines the thermal profile attained within the device and therefore define, in good approximation, device operation. Apart from the Joule heating, also the fundamental thermo-electric interplay between thermal and electrical transport, through the Seebeck property of the materials, contributes significantly to device operation. Fig. 1 illustrates the simplified thermoelectric model.

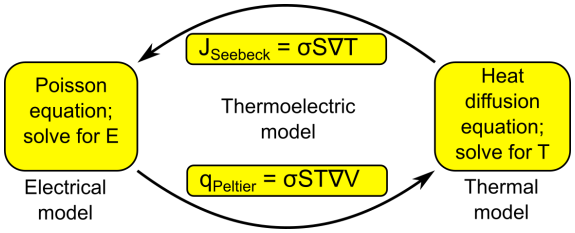

Fig. 1. Coupled thermal and electrical model for PCM modeling. Apart from Joule heating, $q_{Peltier}$ and $J_{Seebeck}$ capture the thermoelectric effects.

1) Thermal model: The thermal model evaluates the temperature distribution within the device according to the thermoelectric power input from the applied electrical pulse, taking into account particularly the additional heat from the Peltier effect. It determines the thermal dissipation paths (the thermal conduction pathways, thermal boundary conditions etc.,) based on the thermal conductivity (κ) of the various materials, the ambient temperature and the interface thermal boundary resistances. The region in the device where the peak temperature is attained is referred to as the "hotspot".

2) Electrical model: The electrical model calculates the electrical potential distribution and the field based on the applied electrical pulse, considering particularly the additional current generated due to the Seebeck effect. PCM devices are known to exhibit a phenomenon known as electronic threshold

978-1-4673-7860-4/15/$31.00 ©2015 IEEE

switching [5], [6]. Therefore it is crucial to take into account the field-dependence of the conductivity of both the amorphous and the crystalline state. After threshold switching, the field is high enough so that the cell is in the so-called "ON state" and the corresponding resistance is denoted as "ON resistance". The thermoelectric power input to the thermal model is mostly determined by the "ON resistance".

3) Thermoelectric effects: It has been reported that the additional thermoelectric heat generated at the interface between the phase-change material and the heater electrode yields a reduction in programming current by 16% [2]. Specifically, a temperature gradient (∇T) induces a current (Seebeck effect), and the potential gradient (∇V) induces a heat flow (Peltier effect). These thermoelectric heating components, all arising from the Seebeck coefficient of the material, are of great interest as, with continued scaling of PCM devices, they will have significant contribution compared with the Joule heating. The Poisson and heat diffusion equations can be modified by the addition of the Seebeck coefficient to include the thermoelectrics and are given by

$$\rho C_p \frac{\partial T}{\partial t} - \nabla(\kappa \nabla T) = \underbrace{\left(\frac{J^2}{\sigma}\right)}_{(Joule)} \underbrace{- J\ T\ \frac{\partial S}{\partial T}\nabla T}_{(Thomson)} \underbrace{- JT\nabla S}_{(Peltier)} \underbrace{- ST\nabla J}_{(Bridgman)} \quad (1)$$

$$\sigma(\nabla^2 V + \nabla(S\nabla T) = 0, \quad (2)$$

ρ denotes the density (Kg/m^3), T the temperature (K), V the Voltage, C_p the specific heat capacitance (J/Kg-K), κ the Th. conductivity (W/m-K), J the current density (A/m^2), σ the El. conductivity (S/m) and S the Seebeck coefficient (V/K).

B. Simulation approach

1) Geometry & boundary conditions: Fig. 2 illustrates the device geometry and dimensions of the mushroom cell topology implemented, making use of the 2-D axial symmetry in COMSOL. The potential is applied at the top electrode and the bottom electrode is assumed to be at electrical ground ($V = 0$). The other outer boundaries are assumed to be electrically insulating such that no current flows across them.

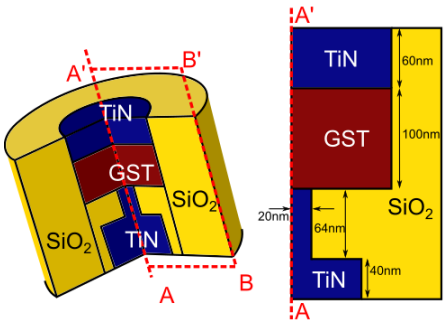

Fig. 2. PCM mushroom topology implemented in COMSOL software with 2D-axial symmetry geometry, with AA' as symmetry axis.

To capture the heat flow across the outer boundaries, a heat-flux boundary condition was implemented that can tuned by a heat transfer coefficient (h) to match the actual thermal resistance of the environment. The heat flux across the boundary is given by

$$q = h \cdot \Delta T; \qquad \Delta T = q \cdot A \cdot R_{th} \quad (3)$$

$$R_{th} \approx \int_{r_s}^{\infty} \frac{1}{\kappa_{th}} \frac{dr}{4\pi r^2} \approx \frac{1}{4\pi r_s \kappa_{th}}; \quad (4)$$

$$\rightarrow h = \frac{\kappa_{th}}{r_s} \quad (5)$$

where q is the heat flux (W/m^2), R_{th} is the thermal resistance (K/W), ΔT is the temperature difference (K), h is the heat-transfer coefficient (W/m^{2}K), κ_{th} is the effective thermal conductivity of the surrounding medium and r_s is the radius of the system (Fig. 3). Combining (3) and (4), h can be estimated using (5) from the effective thermal conductivity of the medium and the radius of the device as input.

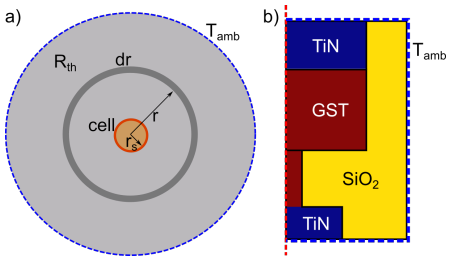

Fig. 3. a) Thermal system with T_{amb} as the ambient temperature. R_{th} is the thermal resistance of the surrounding medium. b) Implementation of the heat-flux boundary condition (dotted blue line) in the geometry studied.

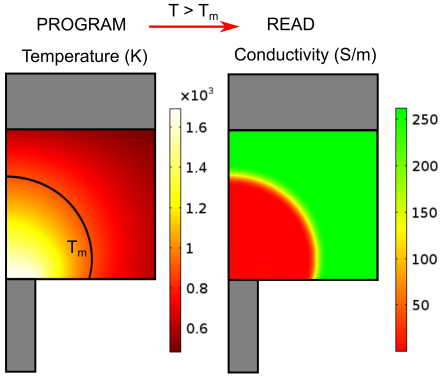

Fig. 4. Simplified programming and read sub-model in COMSOL. Based on the temperature distribution attained while programming, the conductivity is varied in the read sub-model.

2) Programming and read model: To capture the phase-change process, we implemented two separate sub-models (programming and read). The programming sub-model evaluates the temperature based on the applied electric pulse and the temperature-dependent material properties, starting from the crystalline phase. Based on the temperature distribution of the programming sub-model, the material properties are modified in the read sub-model, corresponding to the crystalline ($T_{\text{program}} < T_{\text{m}}$) and amorphous ($T_{\text{program}} > T_{\text{m}}$) states of the phase-change material. Fig. 4 illustrates the sub-models implemented.

III. Material Properties

Both field- and temperature-dependent material parameters are used for GST (Fig. 5). Furthermore, the electrical contact resistance at the GST-TiN interface [7] and the thermal boundary resistances at the GST-TiN and GST-SiO_2 interface are included in the model [8] [9]. The interface Peltier effect was modeled as an additional heat source at the GST-TiN interface.

A Poole–Frenkel-based conduction model is used to capture the exponential voltage dependence of the current typically seen in GST. However, care is taken to implement the temperature dependence with Fermi–Dirac statistics rather than Boltzman statistics to be able to describe also the "ON state", in which the quasi Fermi levels are close to or even within the bands. The thermal conductivity of GST was assumed to follow the Wiedemann–Franz law [10]. The Seebeck coefficient of GST and TiN was calculated using the expression for semiconductors and metals respectively, derived by Mott [11].

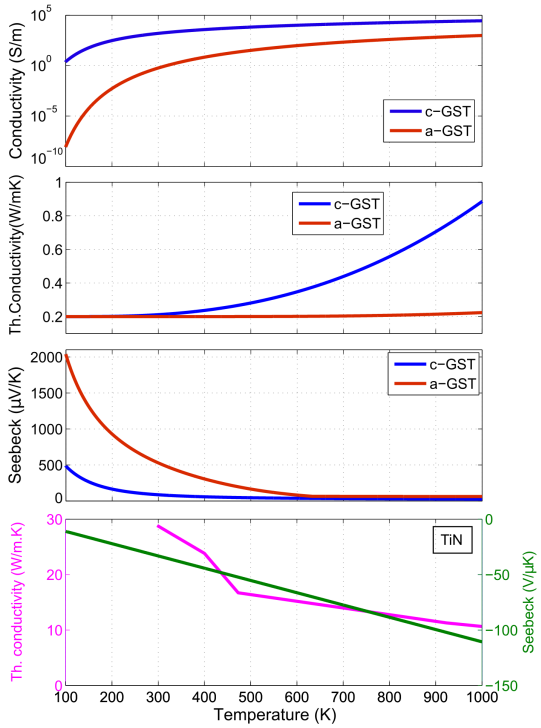

Fig. 5. Temperature-dependent material properties for the crystalline (c-GST) and amorphous (a-GST) state at a field of 1 V/μm. Temperature-dependent thermal conductivity of TiN from [12].

IV. Experimental Setup

Experimental measurements were performed on nano-scale mushroom-type PCM devices. The devices were fabricated in the 90 nm technology node, with the bottom electrode created via a sub-lithographic key-hole process [13]. The phase-change material is doped-GST. The measurements were done under vacuum (average pressure of 10^{-5} mBar) on a JANIS ST-500-2-UHT nitrogen-cooled cryogenic probing station that operates from 77 to 400 K and offers a temperature stability of <50 mK. To achieve temperatures from room temperature up to 400 K, the sample was mounted on an invar block with two embedded tungsten heaters. The temperature was measured using a thermocouple inserted into the invar block and controlled via a Eurotherm temperature controller.

A Keithley 2400 SMU was used for DC voltage or current outputs and the measurement of the corresponding current or voltage at the sample. The device resistance was measured at a constant read voltage of 0.2 V, and the IV characteristics were measured using the current output mode of the SMU from 1 nA to 1 μA.

V. Results and Discussion

A. Temperature profile

The hotspot location plays a critical role in determining the operating efficiency of the device. In the case of mushroom-type devices, the farther the hotspot is from the heater (bottom electrode), the higher is the power required to switch the device. The material properties, thermal boundary conditions, thermal conduction pathways and the device geometry significantly impact the hotspot location and hence the device efficiency. The temperature profile within the device and its dependence on the above-mentioned parameters provide valuable insight for the design of efficient devices.

Fig. 6 represents the thermal profile within the device for different ambient temperatures, but the same applied power of 600 μW. Owing to the difference in ambient temperature (thermal boundary conditions), less power is needed to reach the melting temperature at the rim of the bottom electrode to create a plug leading to a reduced RESET current at higher ambient temperatures (Fig. 9).

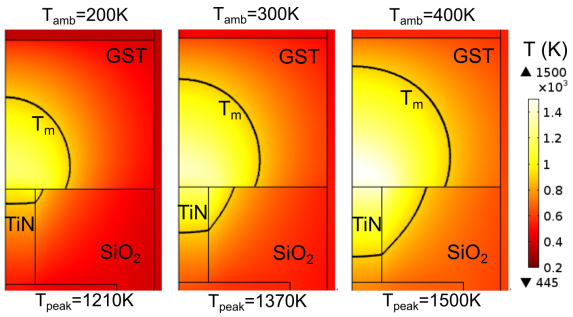

Fig. 6. 2-D thermal profile of the device for different ambient temperatures (200 K, 300 K, 400 K) for the same applied input power of 600 μW. T_m (900 K) is the melting temperature of GST.

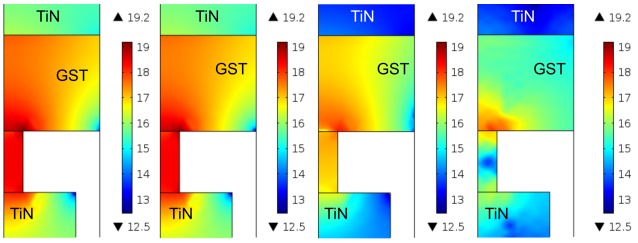

Fig. 7. Individual volumetric heat contributions (W/m^3) from the thermoelectric heating at room temperature for an applied power of 1.1 mW expressed in log scale across the AA'BB' plane in Fig.1. (a) Total heat, (b) Joule heating, (c) Thomson heating, and (d) Bridgman heating.

B. Thermo-electric heating

The individual thermo-electric heating components, as described in (1) are shown in Fig. 7. They are concentrated at the active region closer to the GST-TiN interface owing to the discontinuity in the Seebeck coefficient at the interface (interface Peltier) and the high temperature gradient (Thomson) and current density (Bridgman).

C. Programming $I-V$ characterictics

Fig. 8 depicts the $I-V$ characteristics of the device while programming, starting from the crystalline state and for different ambient temperatures. The conductivity model used for the GST limits the current through the device in the sub-threshold regime. Once the voltage across the GST is above the threshold switching voltage, the resistance of the heater dominates the $I-V$ characteristics. The model is able to capture the current flowing through the device accurately.

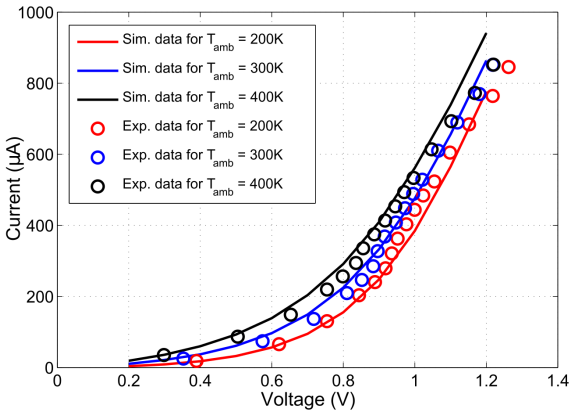

Fig. 8. Programming $I-V$ characteristics for different ambient temperatures (200 K, 300 K, 400 K). Comparison of the simulated and experimental data.

D. Resistance vs. programming power

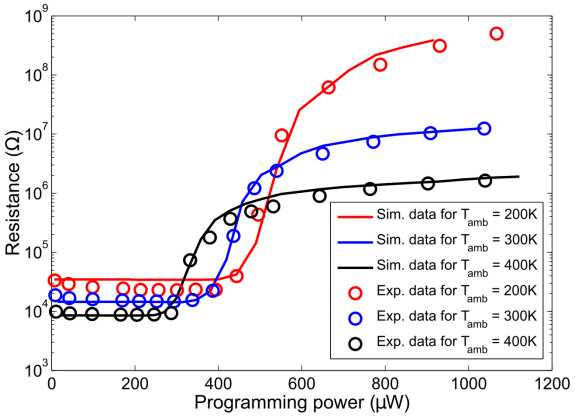

Fig. 9. Resistance vs. programming power for different ambient temperatures (200 K, 300 K, 400 K). Comparison of the simulated and experimental data.

The most commonly used measure for device efficiency is the programming power required to RESET the device (sudden increase of resistance at a certain power). Fig. 9 depicts the measurements and simulation results of resistance vs. programming power for different ambient temperatures. The higher peak temperatures attained owing to the different ambient offset temperatures get translated into lower programming power. This is also in excellent agreement with the experiments performed in Ref. [14]. To achieve a quantitative rather than just a qualitative match, it is crucial to capture both the field and the temperature dependence of the conductivity of GST to properly describe the OFF and the ON state, and to incorporate thermo-electric effects.

VI. Conclusion

We present a comprehensive thermoelectric model that can capture accurately the characteristics of an actual PCM device for a wide range of ambient temperatures. The model provides useful insights for understanding the dominating thermal and electrical transport contributions within the active region of the memory device under the impact of thermoelectric effects. The model is instrumental for a complete understanding of device operation and hence provides valuable feedback for fine-tuning both the material properties and the device design so as to enhance its efficiency.

Acknowledgment

We would like to thank our colleagues at the IBM T. J. Watson Research Center, in particular M. Brightsky and C. Lam, for providing the PCM devices. D. Krebs and A. Sebastian acknowledge funding under the DIASPORA project (ref. 610781) of the FP7-IAPP Marie Curie Action by the European Commission.

References

[1] G. W. Burr *et al.*, "Phase change memory technology," *Journal of Vacuum Science & Technology B*, vol. 28, no. 2, pp. 223–262, 2010.
[2] J. Lee *et al.*, "Impact of thermoelectric phenomena on phase-change memory performance metrics and scaling," *Nanotechnology*, vol. 23, no. 20, p. 205201, 2012.
[3] A. Faraclas *et al.*, "Modeling of thermoelectric effects in phase change memory cells," *IEEE Transactions on Electron Devices*, vol. 61, no. 2, pp. 372–378, Feb 2014.
[4] D. Castro *et al.*, "Evidence of the thermo-electric Thomson effect and influence on the program conditions and cell optimization in phase-change memory cells," in *IEDM 2007*, Dec 2007, pp. 315–318.
[5] A. Pirovano *et al.*, "Electronic switching in phase-change memories," *IEEE Transactions on Electron Devices*, vol. 51, no. 3, pp. 452–459, March 2004.
[6] D. Adler *et al.*, "Threshold switching in chalcogenide-glass thin films," *Journal of Applied Physics*, vol. 51, no. 6, pp. 3289–3309, 1980.
[7] D. Kencke *et al.*, "The role of interfaces in damascene phase-change memory," in *IEDM*, Dec 2007, pp. 323–326.
[8] J. P. Reifenberg *et al.*, "Thermal boundary resistance measurements for phase-change memory devices," *IEEE Electron Device Letters*, vol. 31, no. 1, pp. 56–58, Jan 2010.
[9] J.-L. Battaglia *et al.*, "Thermal characterization of the Sio_2-$Ge_2Sb_2Te_5$ interface from room temperature up to 400°C," *Journal of Applied Physics*, vol. 107, no. 4, 2010.
[10] W. P. Risk *et al.*, "Thermal conductivities and phase transition temperatures of various phase-change materials measured by the 3ω method," *Applied Physics Letters*, vol. 94, no. 10, 2009.
[11] N. F. Mott *et al.*, *Electronic Process in Non-Crystalline Materials*. Oxford University Press, 1967.
[12] J. F. Shackelford *et al.*, *CRC Materials Science and Engineering Handbook, Third Edition*. Boca Raton, FL, USA: CRC press, 2000.
[13] M. Breitwisch *et al.*, "Novel lithography-independent pore phase change memory," in *VLSI Technology Symposium*, June 2007, pp. 100–101.
[14] A. Sebastian *et al.*, "Crystal growth within a phase change memory cell," *Nature Communications*, vol. 5, July 2014.